APPLICATION OF QUANTITATIVE SECOND-HARMONIC GENERATION IMAGING TO DYNAMIC SYSTEMS

BY

MOHAMMAD MAHFUZUL KABIR

THESIS

Submitted in partial fulfillment of the requirements
for the degree of Master of Science in Mechanical Engineering
in the Graduate College of the
University of Illinois at Urbana-Champaign, 2014

Urbana, Illinois

Advisor:

Associate Professor Kimani C. Toussaint, Jr.

ABSTRACT

The purpose of this thesis is to report the development of a quantitative second harmonic generation technique that quantifies the 2 dimensional spatial orientation of collagen fiber samples under dynamic conditions. The technique is demonstrated both for a well aligned tendon sample and a randomly aligned, sparsely distributed collagen scaffold sample. For a fixed signal-to-noise ratio, the applicability of this technique is confirmed for various window sizes (pixel sizes) as well as with using a gridded overlay map that allows for the correlations of fiber orientations within a given image. Additionally, we adapted a graphics processing unit (GPU) to the image analysis with an aim to provide a reduction in image processing time. There, we demonstrate the temporal advantage of the GPU-based approach by computing the number of frames analyzed per second for SHG image videos showing varying fiber orientations. In comparison to a CPU-based image analysis technique, the GPU-based system results in ~ 10x improvement in computational time. This work has direct impact to *in vivo* biological studies by incorporating simultaneous SHG image acquisition and analysis.The adaptation of a GPU to the analysis also introduces this approach to other quantitative, nonlinear imaging techniques.

ACKNOWLEDGEMENTS

I wish to express my most sincere appreciation to my advisor, Professor Kimani C. Toussaint Jr. I learned the importance of diligence and integrity from him. He has helped me reach my accomplishments in the last two years through immense support and guidance. I am especially grateful to Tung Yuen Lau for helping me get initiated in the PROBE lab. He has been my mentor throughout the process and an excellent colleague to work with. I would also like to express my gratitude to the other members of the PROBE lab, namely Dr. VVG Inavalli, Brian Roxworthy, Abdul Bhuiya and Dr. Chen Hao for sharing their knowledge and providing valuable support. Finally, I would like to thank my wife and my family for giving me the encouragement and strength to carry forward this work.

Table of Contents

Chapter 1

Introduction

1.1 Overview

Second harmonic generation (SHG) is a second order nonlinear process where a noncentrosymmetric material – a material with no center of symmetry – converts a part of the incident light to scattered light at twice the incident frequency. The first demonstration of this nonlinear optical technique was performed by Franken et al.[1] in the sixties, which was lateradapted to a nonlinear imaging modality. Even though the initial experiments constituted imaging inorganic crystals [2, 3], the technique soon became popular in imaging biological samples pioneered by the work of Freund and Deutsch to image rat tail tendon [Freund]. Since then SHG microscopy has continued to be recognized as a versatile imaging technique for biological samples, due to its high 3D spatial resolution and high contrast, and specificity to some biological structures, such as myosin and fibrillar collagen[4-6]. Recently SHG has been demonstrated to be an effective and accurate modality to ascertain quantitative information from various collagen-based biological tissues. For example, with respect to collagen fiber organization, the preferred

orientation, and orientation anisotropy have provided significant information. Indeed, these metrics have been applied to obtaining structural information of non-pregnant rat cervical tissue[7], differentiating healthy and injured horse tendon[8], assessing age related changes in porcine cortical bone[9], and quantifying dissimilarities in stromal collagen fiber organization in human breast biopsy tissues at various pathological stages [10].

In spite of the aforementioned developments, a complete applicability of quantitative SHG imaging would require its adaptation to *in vivo* biological processes. To address this, we demonstrate the adaptation of quantitative-SHG (Q-SHG) to dynamic conditions, i.e, computation and display of quantitative information simultaneously with image acquisition.Performing image acquisition and processingsimultaneously provides several advantages over image post processing. Primarily, it provides useful information which allows an user to alter any imaging parameter based on the quantitative information received,while image acquisition is in progress. Additionally, this method could provide added efficiency in disease diagnosis by reducing the feedback time between primary diagnosis and further action. We believe these benefits would prove to be significant for *in vivo* studies.

Recently graphics processing units (GPU) have emerged as more efficient alternate computational devices to traditional CPUs. Due to its inherent ability to provide processing units with parallel computation capabilities, it has gained

widespread usage in computational imaging applications where processing time is expensive [11-13]. With an aim of taking our Q-SHG imaging system towards a video rate analysis, we have incorporated an NVIDIA GPU to our dynamic image analysis technique, enabling parallel processing of the dynamic imaging algorithm. This improvement in processing time makes our approach attractive to other nonlinear imaging modalities that are modified for quantitative analysis.

1.2 Organization of chapters

This thesis focuses on the development and demonstration of a quantitative SHG (Q-SHG) imaging technique under dynamic conditions. Chapter 2 outlines the motivation and the background to developing a Q-SHG technique for dynamic conditions. Chapter 3 focuses on the development and experimental demonstration of the technique to dynamic samples. It includes the methodology of dynamic Q-SHG, its application to tendon and scaffold samples under various dynamic conditions. Chapter 4 elaborates on the adaptation of a GPU to the dynamic Q-SHG technique and discusses in detail on the temporal advantages derived from it. Chapter 5 is the general conclusion of the thesis.

Chapter 2

Background

2.1 Motivation

This section discusses about the motivation behind quantifying the 2D collagen fiber orientation. Collagen constitutes approximately a quarter of the total protein mass of mammals[14, 15]. As a fibrous and insoluble protein it is found in the extra-cellular matrix (ECM) of several significant tissues of the body, such as the cornea, sclera, tendon, bone and skin. [8-10, 14-16]. Among the 20 different types of collagen present in the human body, collagen type I is the most prevalent type. Type I collagen is a fibrillar structure with the ability to withstand strong mechanical loads. The spatial organization of collagen fibers in a particular tissue can determine the type of mechanical property showcased by that tissue. An example of this scenario can be the spatial arrangement of collagen fibers in bones. Bones are functionally graded materials, and so the spatial arrangement of its constituents change over its volume. In compact cortical bones, collagen fibers are packed tightly in concentric rings around each osteon[9, 17]. However a different orientation is observed in trabecular bone, where the fibers are oriented along the longitudinal direction of the trabecula such that the load is transmitted from the diaphysis to the joint along the spongy bone framework in the

epiphysis[17]. Thus, quantification of the spatial organization of collagen fibers in biological tissues is important to study their mechanical properties and functions.

2.2 Quantitative second-harmonic generation imaging

As mentioned in the previous section, Second-harmonic generation (SHG) is a nonlinear optical process. In this process, two input photons of the same frequency are simultaneously obliterated to generate a single photon of double the frequency. Unlike fluorescence, in SHG the signal is generated from a virtual-to-ground state transition, which results in no energy absorption during the process. Therefore SHG has lower photo toxicity when compared to fluorescence. SHG requires a non-centrosymmetric sample being irradiated with a high intensity input beam. As such high contrast images of non-centrosymmetricfibrillar biological tissues can be obtained via SHG microscopy without the necessity for exogenous staining. Because of its minimally invasive requirements for sample preparation and high specificity SHG microscopy has become an increasingly popular technique for imaging collagen-based biological materials.

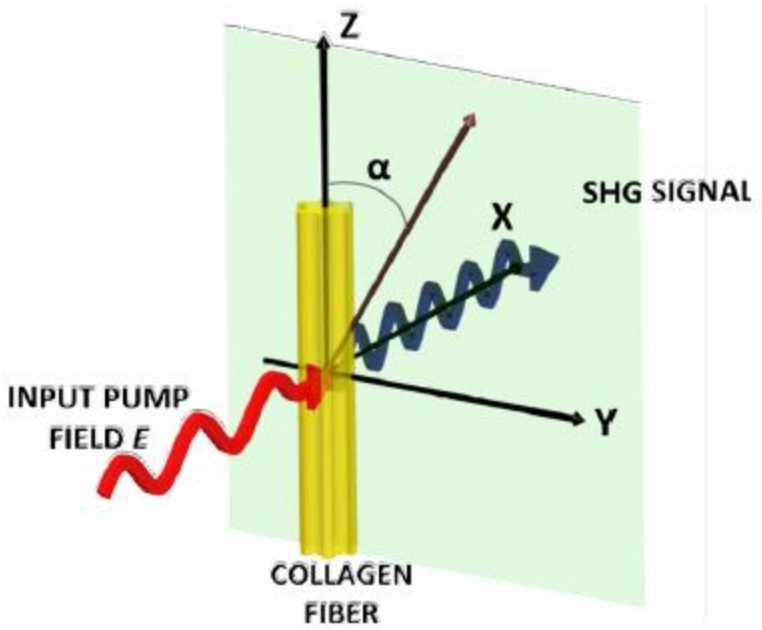

Fig.2.1: Schematic diagram showing second harmonic generation from a non-centrosymmetric collagen fiber [10]

Recently, several efforts have been made to develop quantitative metrics for SHG microscopy. For example, the forward-to-backward SHG intensity ratio have been obtained to provide information regarding the ionic environment of a tissuewhereas polarization SHG has been used to observe alteration in the structure of collagen molecules[18-21]. Apart from these, orientation anisotropy and preferred orientation focus on quantifying the spatial arrangement of collagen fibers with the potential of providing bio-mechanical properties of various tissues [8, 22]. As such, thesemetrics have been used to assess injuries in horse tendon [8], explore age-related changes in porcine cortical bone[9] and to detect spatial differences in collagen fiber arrangement between normal and malignant human

breast biopsy tissues[10]. In view of the promising potential showed by this latter quantitative metric, we have developed an image analysis technique that uses the intensity gradient of image pixels to calculate the preferred orientation and fiber organization.

2.3 Dynamic quantitative second-harmonic generation

To complement the developments obtained in quantitative SHG (Q-SHG) imaging of collagen fibers, a complete applicability of a suchtechnique would require its expansion to dynamic conditions. Even though there have been progress in using SHG imaging for *in vivo* studies [23-25], to our knowledge, there are no reports of dynamic*quantitative*SHG imaging, i.e., computing some quantitative parameters of interest with simultaneous image acquisition. Invariably such a system would present several benefits over a system dependent on post image processing. Performing image acquisition and analysis at the same time would be beneficial to an end user. Based on the quantitative information obtained in real-time the user can choose the parameters of interest, for example, fibers of a particular preferred orientation. In addition this technique would provide a faster method for initial disease diagnosis by reducing the feedback time between primary diagnosis and further diagnostic action. Finally a quantitative

study on a dynamic sample would be significant for *in vivo* studies. Considering these benefits we have applied our Q-SHG technique to dynamic conditions.

Chapter 3

Development of dynamic Q-SHG

3.1 Introduction

3.1.1 Motivation

As mentioned in the previous chapters SHG microscopy has become increasingly recognized in bio-imaging studies for its unique imaging features, namely, high 3D spatial resolution along with high contrast and specificity to some biological structures such as myosin and fibrillar collagen[4-6]. Several approaches have been developed to identify useful quantitative metrics for this imaging modality[26-31]. For example, recently Fourier-transform-second harmonic generation imaging (FT-SHG) has been developed, whereby either 2D or 3D spatial-frequency analysis is used to quantify the spatial organization of structures at cellular scales (300 nm – 100 μm), particularly type I collagen fibers[7-10, 16, 22, 32, 33].These efforts have led to the use of metrics, such as the preferred orientation (of collagen fibers) to differentiate the structure of healthy and injured horse tendons[8] anddetermine structural changes in cortical bone with time[9]. Further efforts have seen the quantification of thediscrepancies in the collagen fiber organization in human breast tissues at various pathological stages[10], and

the development of amethod of obtaining 3D spatial arrangement of collagen fibers, in general, and especially in the cervix[7, 32].

3.1.2 Background

Notwithstanding the appreciable developments in quantitative SHG imaging, their extension to dynamic situations is required for its complete applicability to biological samples. Even though SHG imaging has been used for *in vivo* studiespreviously [23-25], there has been no known reports of real-time *quantitative* SHG imaging, i.e., presenting quantitative parameter(s) of interest with simultaneous image acquisition. The simultaneous operation of these two processes would allow the user to alter imaging parameters while imaging to suit the necessity.Quite clearly, this type of a modality would greatly enhance imaging quality and prove to be important for *in vivo* studies. In addition, simultaneous image acquisition and processing could potentially translate into added efficiency in disease diagnosis by reducing the feedback time between various stages of disease diagnosis.

3.1.3 Dynamic Q-SHG

With an aim to adapt quantitative SHG imaging to eventual *in vivo* biological studies, we examine the experimental conditions that permit quantitative SHG imaging under dynamic conditions. We look at two extreme conditions of test samples: stained tendon with well-aligned, highly organized collagen fibers and unstained, synthesized collagen scaffold. Using these samples, we apply quantitative SHG imaging to two dynamic situations. The first determines fiber-orientation information as the samples are spatially scanned in a plane. The second situation computes the same information for a collagen gel sample as it dries to form a 2D collagen scaffold assembly. The 2D intensity gradient method (which is applied to the intensity of the images in real-space) is employed to calculate the preferred orientation. Furthermore, we apply our approach to an example application to image and quantitatively analyze stromal collagen fibers belonging to individual cores in a standard breast tissue microarray (TMA) sample as they are progressively stage scanned, and where each core has been clinically classified as either benign or malignant.

This chapter is organized in the following way: section 3.2 describes the sample preparation, experimental setup, and quantitative measures used. Section 3.3 presents the results and discussion, while section 3.4 gives the conclusion briefly summarizing our observations.

3.2 Methods

3.2.1 Sample preparation

Tendon, collagen scaffold, and tissue microarray samples were used in this study. Porcine tendon tissues were obtained from a local abattoir and embedded and preserved in OCT compound at -80° C. Next, the samples were brought to -20° C and 4-μm thick sections were cut using a cryostat (Leica CM3050S). They were then thawed and stained with a hematoxylene and eosin (H&E) stain. Finally, each tissue section was mounted with a permanent mounting media (Permount) onto a microscope coverslip (No 1.5).

The procedure for synthesizing the collagen scaffold follows closely to that described in the literature[34]. High concentration type I collagen solution (BD Biosciences) was extracted from rat tail tendon. A solution of 50 μL of 10x PBS was added to 426 μL of ultra-pure H_2O, followed by 0.5 μL of 1 N NaOH and 23.5 μL of collagen solution. The components were mixed in an eppendorf tube, sealed and refrigerated at 4° C for 24 hours. During experimentation, 10 μl volumes were transferred onto a coverslip for imaging.

A breast tissue microarray sample (US Biomax BR1003) was obtained from formalin-fixed, paraffin-embedded tissue. The sample comprised 1-mm diameter, 5-μm thick, cores of histologically variant classes of tissues (e.g., normal,

dysplastic, and malignant). The samples were stained with H&E and mounted with xylene mounting medium onto a microscope coverslip (No 1.5).

3.2.3 Experimental setup & image analysis

Figure 3.1(a) shows the schematic of the experimental setup used for the purpose of this study. All experiments were carried out with a spectrally tunable, Ti:sapphire pulsed laser (Spectra-Physics Mai-Tai HP DeepSee), producing 100-fs duration pulses with 80-MHz repetition rate. The excitation wavelength used in this study is spectrally centered at 780 nm, and a combination of half-wave plate and polarizer are used to control the input power. A pair of galvanometer-based scanning mirrors (GVS012, Thorlabs) is used to scan the beam over a desired rectangular area. Scanning incorporates two triangular patterns of the same amplitude but with frequencies that are not harmonically related. This ensures, fast and uniform illumination over the entire scanned area. Next, the scanned beam is reflected by a short pass, 670-nm dichroic beam splitter, and subsequently focused onto the sample using a 1.4 NA oil-immersion objective lens (Olympus U Plan S Apo 100x). The backward emitted SHG signal is collected by the same illumination objective followed by a laser-blocking filter (Semrock FF01-680/sp-25) and an SHG filter (Semrock FF01-390/18-25). The signal is captured using an

EMCCD camera (Hamamatsu EM-CCD C9100-13) with a total pixel area of 512 x 512 with a constant EM gain of 100x for all images.

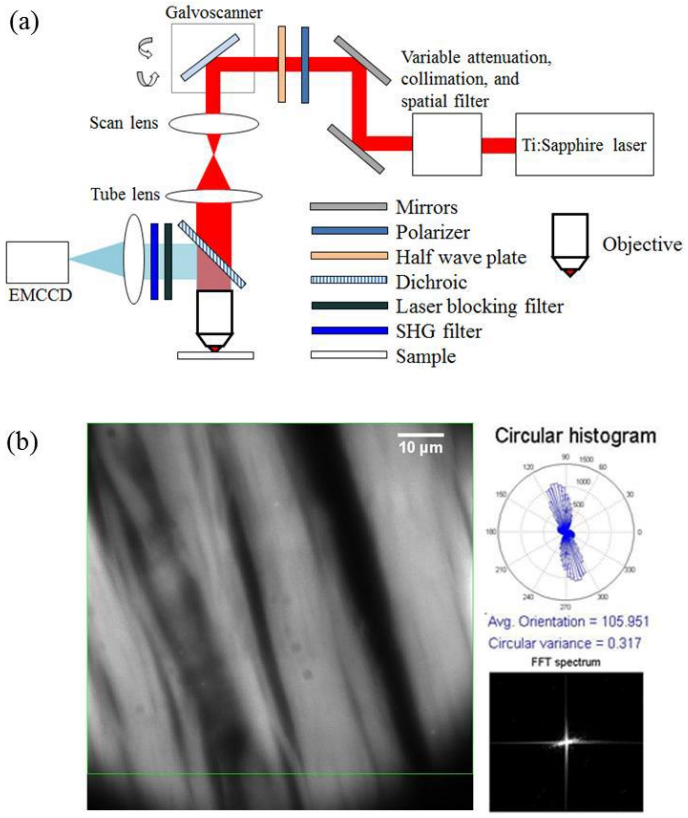

Fig. 3.1: (a) Schematic of the experimental setup used and (b) an example SHG image of stained tendon sample with associated circular histogram (top right) and FFT spectrum (bottom right). See text for details.

Figure 3.1(b) displays the interface used for the real-time quantitative SHG analysis. Continuous frames of 512 x 512 pixel images are captured by the EMCCD camera and displayed on the screen. A customized MATLAB code

permits simultaneous data analysis with image capture. A 2D intensity gradient method[35, 36] is employed to determine the fiber orientation. First, a region of interest (ROI) is identified (outlined by the green rectangle). Next, the preferred fiber orientation at each pixel within the ROI is obtained by calculating the local intensity gradient and the result is subsequently depicted in the form of a circular histogram [Fig. 3.1(b), top right corner]. The associated circular variance, which varies from 0 to 1, renders a quantitative measurement of orientation isotropy, and information about it can be found elsewhere[37, 38]. An FFT spectrum of the ROI is also displayed [Fig. 3.1(b), bottom right corner], which can be used to directly determine preferred fiber orientation[33].

3.3 Results and discussion

In order to determine the capabilities of our approach under dynamic conditions, we first examine the application of quantitative SHG for two sample types for various imaging areas. Specifically, we estimate the acquisition time and processing time as a function of input power, sample type, scan area, fiber density, and desired signal-to-noise ratio (SNR). Figure 2 summarizes the results of this experiment, where (a) corresponds to images of tendon and (b) images of collagen scaffold for window sizes (green box) referring to (i) 120 x 120 (ii) 240

x 240 (iii) 360 x 360 and (iv) 512 x 512 pixels. As mentioned earlier, these two sample types are representative of two of the more extreme conditions: well-aligned, highly organized, dense (stained) collagen fibers, and randomly aligned, fairly disorganized, more sparse (unstained) collagen fibers. To make any comparison between the two image types feasible, an SNR of 7 is maintained for both samples by using an input power of ~ 3 mW and 40 mW for the tendon and scaffold samples, respectively. In terms of the fiber orientation analysis that is typical for quantitative SHG, it is clear from Figs. 3.2(a) and (b) that a change in the window size does not bring about any significant changes in the preferred orientation results (indicated at the bottom of each image). Indeed, we observe across all window sizes, the circular variance is lower for tendon than scaffold, consistent with the fact that the latter is a more randomly aligned sample. Figure 3.2(c) depicts the acquisition time per window size for each sample, ranging from ~ 400 ms to 6 sec. Note that although the EMCCD camera can capture a frame in ~ 32 ms, we use much longer image acquisition times to account for the low conversion efficiency of second-harmonic generation[39]. In addition, we confirm that the acquisition time scales with window size for the first three pixel areas; however, for 512 x 512 pixels, more than 4x the base window size (120 x 120), the corresponding acquisition time is ~12x longer. This comes from the fact that the average power is distributed over a larger area, and thus, the corresponding laser dwell time per point needs to increase in order to generate SHG. Therefore,

it is expected that for increased window sizes and fixed input power, the acquisition time will increase in order to maintain the same SNR between various window sizes. Finally, Table 3.1 presents the processing time required for each image size for each sample. The time is observed to scale with both the image size and the distribution of fibers on the image, as can be observed for tendon and scaffold images of the same size; hence, for the same pixel area, tendon sample requires a longer processing time compared to the sparsely distributed scaffold sample. It should be noted that the three parameters considered, namely, imaging window size, SNR, and acquisition time, are all interdependent. For our purposes, we have chosen the SNR to be the fixed parameter since we believe it to be the more pragmatic choice to a microscope user.

Using the information summarized in Fig. 3.2 and Table 3.1, we next consider two dynamic situations. A video of the first case was constructed(Media 3.1), select frames of which are shown in Fig. 3.3(a). Here, the tendon sample is scanned by moving the stage laterally in 5-μm steps [relative to the initial position (0, 0)] in arbitrary directions, the lateral coordinates (x, y) of which are shown in the bottom, right-hand corner of each image. The window size used here is 240 x 240 pixels, with an acquisition time of 1.2 s per location and a fixed input power. The preferred orientation and circular variance are computed simultaneously as the sample is scanned. The same procedure is repeated and captured in a video(Media 3.2) for the collagen scaffold sample, select frames from which are

shown in Fig 3.3(b). A 1.2 s acquisition time per location is also used here, with an adjusted input power of 40 mW. Overall, we observe that ~2s is required for image acquisition and processing; therefore, dynamic processes that are of the order of 2s or longer can be simultaneously captured and analyzed (using our metrics) without any tradeoffs. Again, we observe that for the case of collagen scaffold, the circular variance is almost twice that of tendon.

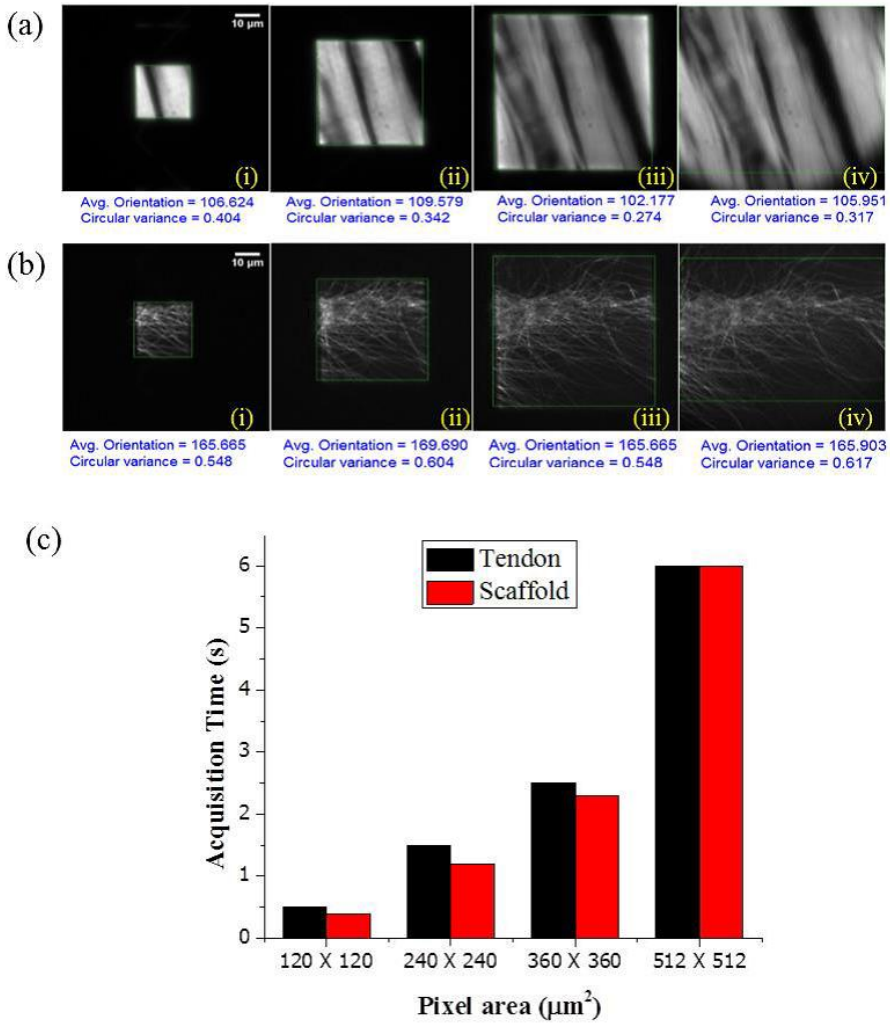

Fig. 3.2: SHG images of (a) tendon and (b) collagen scaffold fibers for various pixel areas and a fixed SNR of 7. The corresponding pixel areas are: (i) 120 x 120 (ii) 240 x 240 (iii) 360 x 360 and (iv) 512 x 512 pixels. The same scale applies to all images. (c) The acquisition time for each image area is plotted against the pixel area.

Table 3.1*Image processing time for various image sizes.*

Image Area (Square pixels)	Image Processing time (ms)	
	Tendon	*Scaffold*
120 x 120	420	280
240 x 240	570	430
360 x 360	680	570
512 x 512	950	750

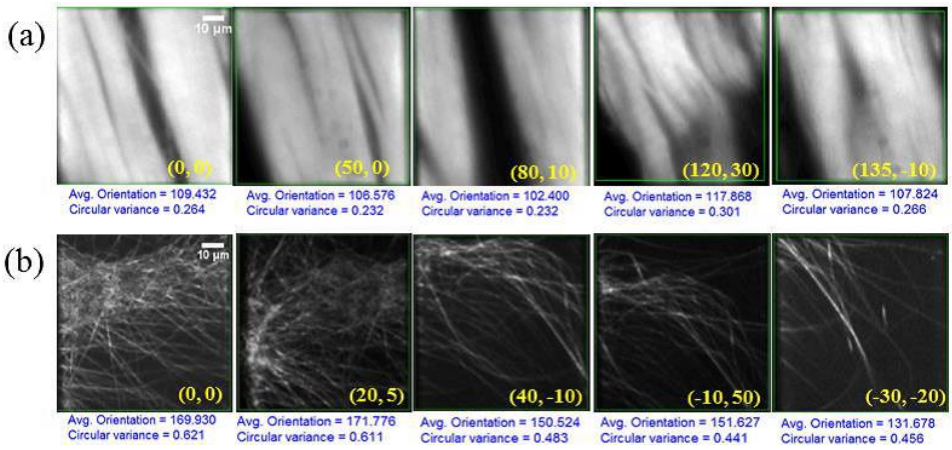

Fig. 3.3: SHG images of stage-scanned (a) tendon (Media 3.1) and (b) collagen scaffold fibers (Media 3.2) at different locations. The lateral coordinates for each image, relative to the initial (0, 0), are provided in the bottom right hand corner for each frame. The same scale applies to all images. See text for additional details.

For the second dynamic situation, we attempt to carry out quantitative-SHG imaging of a collagen gel solution in real time, as it dries at room temperature (~23°C) over a period of 30 min. In this case, 10 µL of solution dries to form a 2D

collagen fiber layer on a microscope coverslip. To visualize this process, the objective lens is focused on to the bottom of the coverslip. A video (Media 3.3) is captured and select frames are shown in Fig. 3.4. Initially, blurred images are observed, consistent with the fact that collagen fibers occupy a 3D volume, causing SHG signals to be generated and scattered from various layers within that volume. As the fibers begin to settle down, the SNR increases [see Fig. 3.4 (ii)-(iv)]. In addition, we confirm that the preferred orientation and circular variance, our metrics of interest, can easily be computed during drying; note that the circular variance decreases with time as more defined fiber structures become visible. It is worth mentioning here, that collagen scaffolds are extremely important to many areas of tissue and bioengineering, especially for bone repair applications. An approach that noninvasively monitors the drying and assembly of such fibers *in situ*, while simultaneously quantifying fiber organization would be attractive to these fields, and could ultimately facilitate new strategies in fiber scaffold design.

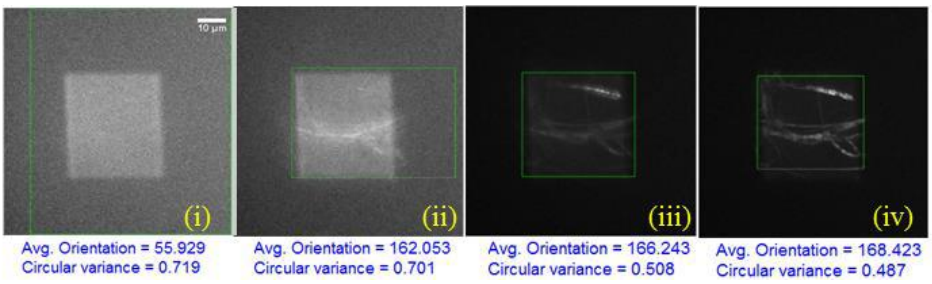

Fig. 3.4: SHG images of collagen scaffold fiber formation (Media 3.3) at different times in (i) 10 (ii) 11.4 (iii) 11.6 (iv) 12.2 minutes. The same scale applies to all images.

It is interesting to consider how our approach may be useful in a clinical setting. Let us consider a scenario where a pathologist would be interested in analyzing several tissue biopsies (e.g., breast or skin samples) for malignancy. It would be tremendously useful to be able to simultaneously image and analyze each sample in order to promptly make an initial recommendation. To simulate such a scenario, we next apply quantitative SHG to stromal collagen fibers from breast tissue biopsies from various cores in a TMA as the cores are continuously stage scanned; such TMA slides offer clinical compatibility and are used for gold-standard histopathological diagnosis of cancer. FT-SHG has previously been applied to such tissue cores, where it was found that there exists clear differences in regularity of fiber orientation between healthy and malignant tissues. Specifically, malignant tissues generally have well-directed, organized fibers, and healthy tissues exhibit significantly more random organization[10]. In an effort to adapt our simultaneous imaging and quantitative analysis method to capture this

difference in fiber orientation, we have applied a gridded overlay map for each image as we moved from one core to another of a TMA, to allow for potential correlation analysis between fibers from different spatial regions within the same image. A video (Media 3.4) is captured and two representative frames are shown in Fig. 3.5. Here we use 10 mW of average power, 1.2 s acquisition time, and 512 x 512 pixel area comprising an 8 x 8 grid (and thus each grid contains 64 pixels). Details on 2D quantitative-SHG analysis to calculate localized fiber orientation can be found elsewhere[22]. The processing times varied from 300 to 800 ms depending on the density of fibers. We confirm in Fig. 3.5 (and the accompanying video) that malignant tissues generally have well-directed, organized fibers, and healthy tissues exhibit significantly more random organization[10].

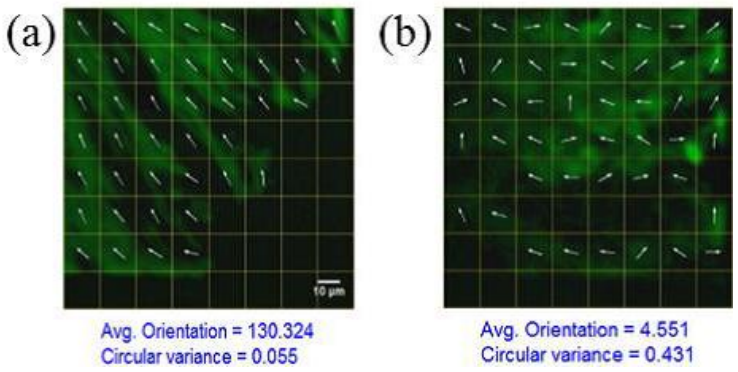

Fig. 3.5: SHG images of breast tissue samples (Media 3.4) at different cores corresponding to (a) malignant (b) healthy tissues. The same scale applies to all images.

3.4Conclusion

Q-SHG has beenapplied to several dynamic situations and quantitative metrics of interest were calculated. Primarily we have considered two extremes of collagen sample types: well-aligned, dense (stained) tendon samples and sparsely distributed, randomly aligned (unstained) collagen scaffolds. We first established the minimum acquisition time for a fixed input power and SNR of 7, and for various window sizes (pixel areas) ranging from 120 x 120 to 512 x 512 pixels. The acquisition time scaled linearly with window size for small to moderate pixel areas, and increases nonlinearly for the maximum pixel area due to increased laser dwell time necessary to generate an SHG signal. Quantitative metrics such as preferred fiber orientation and circular variance can be computed simultaneously for each sample as an SHG image is acquired. In one case, we computed the aforementioned metrics for each sample during lateral stage scanning. Here, we established that for a window size of 240 x 240 pixels, average input powers of 3 mW and 40 mW were required for the tendon and collagen scaffold samples, respectively, with a corresponding minimum acquisition time of 1.2 s per frame and a processing time from ~ 500 to 700 ms depending on the density of fiber distribution. For the second dynamic condition we again determined the desired quantitative metrics during a collagen gel drying process. We observed a progressively smaller degree of circular variance as the fibers dried and assembled on the coverslip. Our approach was also applied to a simulated clinical

scenario by demonstrating quantitative SHG imaging on regularly, stage-scanned breast tissue cores in a tissue microarray sample. By analyzing localized fiber orientations for each imaged area, we showed that it was possible for our approach to discern between healthy and malignant tissues under this dynamic condition. We believe that our approach has potential application to real-time imaging of other noncentrosymmetric biological structures such as axons for neuroimaging studies[40], and collagen fibers during cervical remodeling for studies of premature birth[7].

Chapter 4

Adaptation of GPU to dynamic Q-SHG

4.1 Introduction

4.1.1 Background

In the previous section we presented the experimental and computational requirements for performing Q-SHG imaging under dynamic conditions [41]. It is clear from the discussion that the computation time appears to be a substantial portion of the total procedure and its reduction would provide significantly more quantitative information from the imaging system. Recently graphics processing units (GPUs) have emerged as alternate computation devices for faster processing compared to standard CPUs. Such GPUs comprise several thousand times more processing units or cores compared to conventional computer CPUs, thereby permitting all cores to be used to carry out the same desired instructions in parallel. This facilitates its usage in various computational imaging applications, where processing time is expensive. For example, GPU-based algorithms have been used to develop spectral domain and fourier domain optical coherence tomography[11-13] techniques with significant reduction in computation time

when compared to standard CPU-based algorithms. Similar results have also been observed from using the GPU for reconstruction of X-ray computed tomography (CT) images of high contrast and precision [42] as well as performing deconvolution of 3D confocal microscopic images[43]. As such, the GPU would be extremely useful in obtaining quantitative information in real-time from fast dynamic imaging applications such as observed in *in vivo* biological processes.

4.1.2 GPU-based dynamic Q-SHG

In our discussion on the experimental and computational parameters for dynamic Q-SHG imaging, we found that for a 512 x 512 pixel area, the preferred orientation of collagen fibers in a densely organized tissue specimen captured by SHG imaging can be computed within ~ 950 ms using a standard multi core CPU. With an aim to obtain significant improvement in computation time, we incorporate an NVIDIA GPU to our image analysis system, enabling parallel processing of our dynamic SHG image analysis algorithm. As proof-of-concept, we designed several synthetic experiments, whereby we applied our GPU-based approach to quantitatively analyze consecutive frames from several videos of 512 x 512 pixel SHG images. In general, the videos are of varying arrangements of collagen fiber organization. We compare the computation time obtained using GPU versus CPU. Thischapter is organized as follows : section 2 describes the

experimental methods and image analysis technique used. Section 3 presents the results and discussion, while section 4 provides the conclusion to this chapter.

4.2 Methods

4.2.1 Image Analysis

We have previously provided a detailed description of our quantitative SHG image analysis carried out under dynamic conditions, which can be found elsewhere[41]. Briefly, after acquiring a 512 x 512 image, a Gaussian filter is applied and the image is subsequently divided into a 16 x 16 grid, whereby each grid contains 32 x 32 pixels. For each grid a preferred orientation is calculated based on the computed intensity gradient for each pixel within a grid. This information can then be used to estimate a global preferred orientation for the whole image. The accuracy of the calculated orientations is estimated by calculating the circular variance[35-38], a detailed description of which is provided in Appendix A. An intensity threshold is set to discriminate background from signal in a manner analogous to what we have previously reported[22]. This same threshold is used for calculations that are done both within a grid and for the global orientation estimate. Finally, an image is displayed with a gridded overlay,

with arrows indicating preferred fiber orientation within each grid and the computed average orientation and circular variance being presented.

MATLAB coupled with Compute Unified Device Architecture (CUDA) parallel computing platform was used to develop this code. The parallel instructions were written in C programming language, using the NVIDIA CUDA library version 5.0[44], and implemented in the GPU while MATLAB was used as the host function to acquire the image, transfer image data to and from the GPU, and subsequently display the results. The hardware used for implementation consisted of an NVIDIA GTX 590 GPU, running on a Windows 7, Core i7-2600K processor with 32 GB RAM. This same computer was used for the comparisons where GPU-based calculations were compared with CPU-based ones. A description of the GPU architecture and the CUDA programming model can be found in the CUDA Programming Guide 5.0 [44]. To facilitate its adaptation in the GPU architecture, the image analysis procedure was divided into three segments known as CUDA kernels as shown in Fig. 1. In the first kernel, the acquired 512 x 512 image is divided into a 43x43 grid, each of which is 12x12 pixels in size. For this kernel, the GPU grid contains 43x43threadblocks, where each threadblock in the grid contains 16x16 threads. Each threadblock is assigned to apply a Gaussian filter over one image grid. As the pixels in the boundary of a grid require contributions from neighboring pixels to apply the Gaussian filter, the threadblocks contain one extra thread in each boundary. In the second kernel, the

filtered image is divided into a 16x16 grid of 32x32 pixels each, whereby the preferred orientation is calculated for each individual grid. In both these two kernels individual GPU threadblocks are assigned to individual image grids, where individual pixels inside the grids are computed upon by individual threads in the threadblock; hence, parallel operation of data points is achieved on two separate levels. On the first level, all the threadblocks in the GPU multiprocessors carry out their computation in parallel, while on the second level, the individual threads inside a threadblock also operate in parallel. This essentially means all pixels in a grid, and all grids in the image are computed upon simultaneously, thus reducing our computation time significantly. Finally, in the third kernel, the preferred orientations from the individual grids are used to calculate a global preferred orientation. As there are only 256 (16x16) preferred orientation values, a single GPU threadblock of 256 threads is sufficient. After performing the processing in the GPU, the image along with the quantitative information is returned to the CPU. MATLAB instructions are used to display the preferred orientation in each block of the 16x16 grid and a circular histogram showing the distribution of the preferred orientation values over the complete image. The global preferred orientation and the circular variance is also displayed.

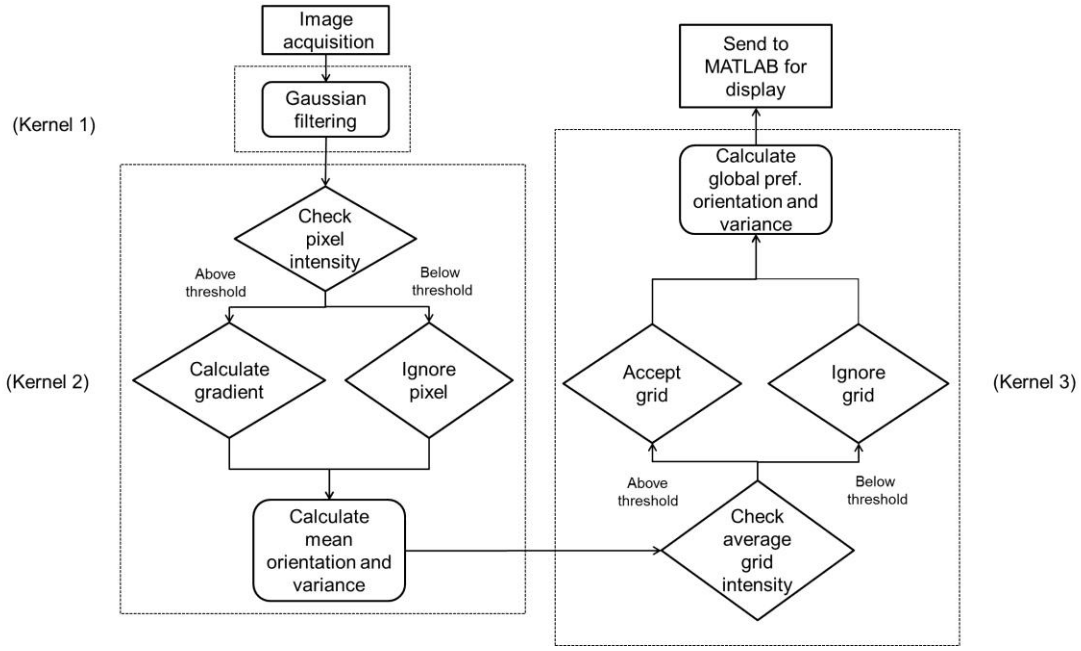

Figure 4.1: Flow chart of the steps performed in the GPU-based quantitative image analysis modality.

4.2.2 Experiment

Both the GPU-based and the CPU-based code are applied on consecutive frames of three videos comprising 512x512-pixel SHG images. In the first video, we have consecutive frames showing SHG images of breast biopsy tissue being rotated at increments of 20° (relative to the horizontal) between each frame. The frame rate of the video is 10 frames per second (fps) and contains 20 images running for a total duration of 2 seconds. The contents and distribution of the second video is the same as the first one, except that the frame rate of the video is set at 33fps. The third video is of SHG images of various collagen-based

biological tissues, namely porcine tendon, rat cervix, and breast biopsy tissues. The frame rate is set at 10 fps, while the number of images and total run time is set at 20 images and 2 seconds respectively.

4.3. Results and Discussion

Figure 4.2 depicts the representative frames from the first video, as well as the results obtained by operating the two different computational modalities on it. Figure 4.2(a) shows the first 6 frames of the video, while Figs. 4.2(b) show the frames that are captured and analyzed by the GPU-based and CPU-based codes in two consecutive rows, respectively. It is clear from Fig. 4.2(b) that the GPU-based code successfully captures and analyzes all 6 consecutive frames of the video. For the given frame rate, this is consistent with the expected computation time of ~ 100 ms for each image. In comparison to this result, the CPU-based code only acquires the first frame, and fails to capture any of the subsequent frames. This observation supports our previously reported fact that the computation time for a CPU-based code is ~ 950 ms for a 512 x 512 pixel image[41], indicating that at 10 fps it would fail to capture the next 9 consecutive frames. The same analytical steps were carried out for the second sample video, the results of which are depicted in Fig. 4.2(c). The two consecutive rows in Figs. 4.2(c) shows the frames

that are captured by the GPU-based and CPU-based modalities respectively. It is observed from Fig. 4.2(c) that for the new video frame rate of 33 fps, the GPU fails to capture two out of every three frame of the video It is also observed from the second row in Fig. 4.2(c) that the CPU based code could only analyze the first frame in this case too, and fails to capture any subsequent frames.

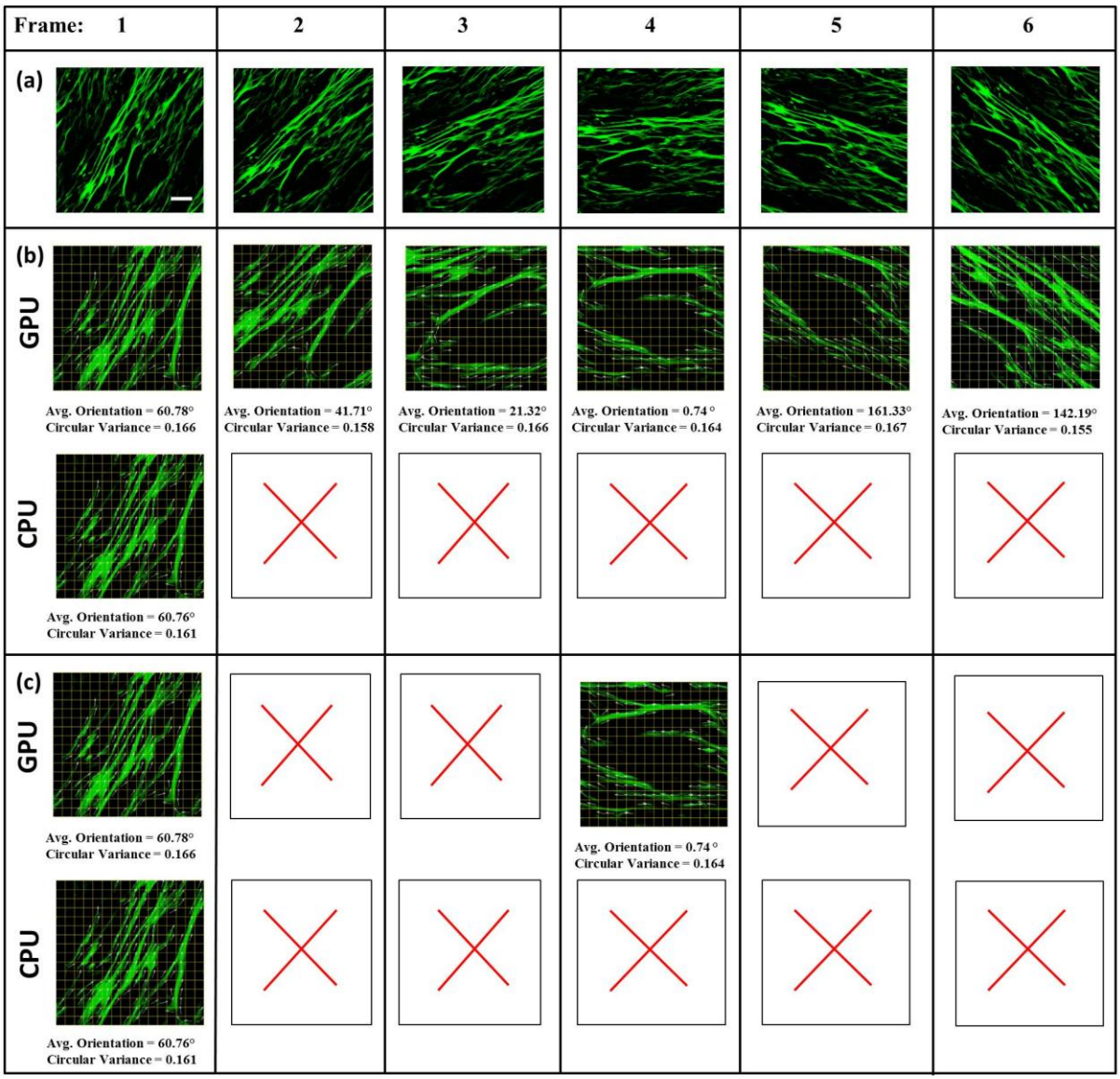

Fig. 4.2: Representative frames from a video of SHG images of breast biopsy tissues. (a) The first 6 consecutive frames in the video, showing fibers that are progressively rotated by 20° with respect to the horizontal. Among these, the actual frames captured and analyzed by the GPU-based and CPU-based image analysis are shown in (b), where the video frame rate is 10 fps. (c) shows the actual frames captured and analyzed by the GPU-based and CPU-based image analysis when the video rate is changed to 33 fps. The scale bar corresponds to 10 μm for all images. These results are also compiled in the videos (Media 4.1)and(Media 4.2). See text for additional details.

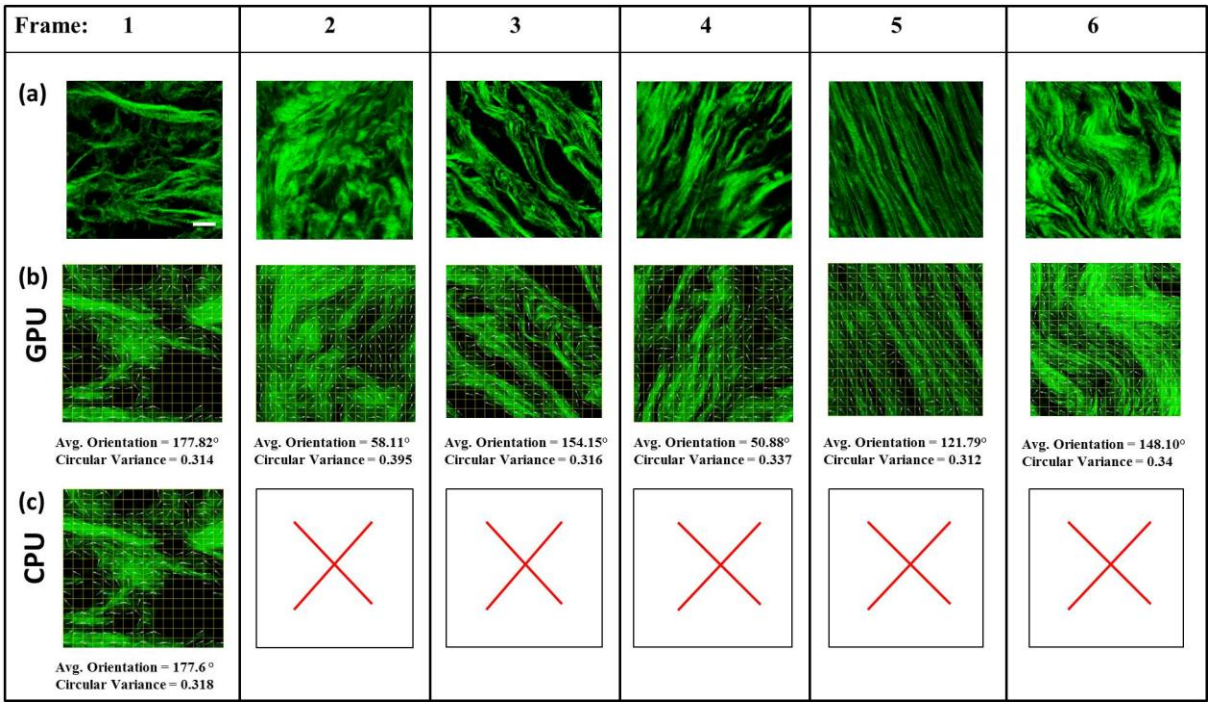

Fig. 4.3: Representative frames from a video of SHG images of several collagen-based tissues (a) Frames 1, 3, and 4 are images of human breast biopsy tissues, while frames 2, 5 and 6 are of rat cervix and porcine tendon tissues, respectively. (b) and (c) show the frames captured and analyzed by the GPU-based and CPU-based codes, respectively. These results are also compiled in a video (Media 4.3). The scale bar corresponds to 10 μm for all images. See text for additional details.

Figure 4.3 shows the results obtained from analyzing consecutive frames of a video comprising of SHG images of a variety of collagen based tissues. Here, the goal is to evaluate the performance of the GPU-based code when SHG images vary (in fiber density, orientation and organization) greatly between each consecutive image. Again, we observe in Fig. 4.3(b) that the GPU-based code

captures and analyzes all consecutive frames from the video irrespective of fiber orientation or density, while in Fig. 4.3(c) we see that the CPU-based code could only perform its analysis on the first frame. Thus, the processing time for the GPU-based approach is not influenced by fiber density and spatial organization.

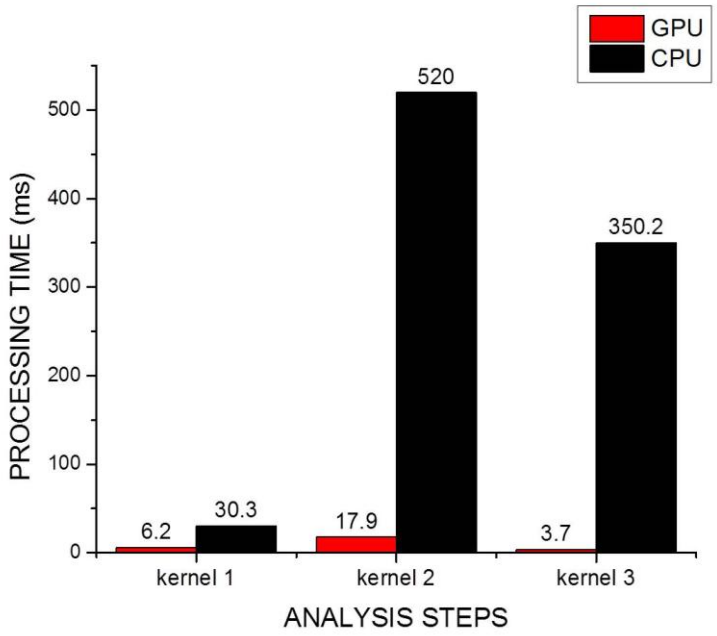

Fig. 4.4 : Image processing time required for the GPU-based analysis compared with the CPU-based analysis for three different analysis steps.

Figure 4.4 compares the performance in processing time between GPU and CPU-based approaches for each segment of the analysis. To get an accurate estimate of the processing times, the two modalities are used to analyze 20 SHG images of

size 512x512 pixels showing varying degrees of fiber organization and density. The processing time for each step for all the images are obtained and their average values are used in this comparison. It is observed from Fig. 4.4 that the calculation of the preferred orientation of individual image grids (kernel 2) takes the longest amount of time for both approaches. As such, to obtain a significant reduction in overall computation time, it would be important to reduce the time required by kernel 2. Our GPU-based implementation achieves a time improvement of ~ 20x for kernel 2, reducing it from ~ 520 ms using CPU to ~ 18 ms. Application of a Gaussian filter and calculation of global preferred orientation were performed ~ 5x and ~ 35x faster, respectively. The time required to display the results (not shown) is the same for both the modalities and it was observed to be ~ 50 ms. Overall the GPU-based code performs the analysis at an average of ~ 10x faster than the CPU-based code.

It is worth noting that although 512 x 512 pixel images were used for the proof-of-concept, the GPU-based code can also be used to analyze images of larger pixel sizes without any modification. The image grid size and the number of threadblocks in the GPU would scale according to the image size. Individual image grids and threadblocks would also contain the same number of pixels and threads, respectively. In certain cases, the individual image grid sizes may need to be increased to facilitate clear visualization. This would require each thread in a threadblock to process more than one pixel. For example, if the image grids

contains 64 x 64 pixels, a threadblock of 32 x 32 threads would assign one thread to analyze data obtained from four pixels. Note that this would require an increased amount of memory in the GPU which is not supported in the current version of the GPU that was used in this work. Apart from this, if any further quantitative analysis is desired from the SHG images, additional CUDA kernels could be constructed, which can be conveniently added to the existing code.

4.4. Conclusion

In this paper, we demonstrated a GPU-based quantitative analysis of SHG images. We showed that the preferred orientation of collagen fibers can be determined in ~ 100 ms, either at the level of individual elements in a 16 x 16 grid or globally for a 512 x 512 pixel image. As proof-of-concept we have applied this modality to analyze consecutive frames of two videos of 10 and 33 frames per second, respectively. In the first case the GPU-based system successfully captured and analyzed all the frames of the video, while in the second case it succeed in capturing one in every three frame. In contrast, the same analysis using a standard CPU failed to capture all but the first frame in both the videos. Both approaches were again compared for a video of SHG images from more complex, collagen-based structures, with the GPU-based method clearly outperforming the standard

method. This improvement in processing time makes our approach attractive to other nonlinear imaging modalities that are modified for quantitative analysis.

Chapter 5

Conclusion

This thesis has reported the development of a quantitative second harmonic generation technique that quantifies the 2 dimensional spatial orientation of collagen fiber samples under various dynamic conditions. Primarily two extremes of collagen sample types were considered, namely the well-aligned, densely packed (stained) tendon samples and sparsely distributed, randomly aligned (unstained) collagen scaffolds. We first established the minimum acquisition time required for a fixed input power and SNR, along with varying window sizes (pixel areas) ranging from 120 x 120 to 512 x 512 pixels. It was observed that the image acquisition time increased linearly with window size but only for small to modest pixel areas. Due to increased laser dwell time necessary to generate SHG signals the acquisition time scaled nonlinearly for the maximum pixel area. We computed our quantitative metrics of interest, such as preferred fiber orientation and circular variance simultaneously for each sample,while an SHG image is acquired. Our experimentation with each sample type during lateral stage scanning established

that significantly large differences in input power requirements were observed for the sparsely distributed and densely packed sample types, corresponding to the same image acquisition time of 1.2 s per frame. For a second dynamic condition we again determined the desired quantitative metrics during a collagen gel drying process. We observed a progressively smaller degree of circular variance as the fibers dried and assembled onto the coverslip. With an aim to adapt our technique to a clinical setting, we applied the dynamic imaging modality to a simulated clinical scenario. This was performed by demonstrating quantitative SHG imaging on regularly, stage-scanned breast tissue cores in a tissue microarray sample. By analyzing localized fiber orientations for each imaged area, we showed that it was possible for our approach to discern between healthy and malignant tissues dynamic conditions.

Additionally, we have incorporated a graphics processing unit (GPU) into our image analyzing modality to significantly reduce the computation time. In this thesis we also presented the results obtained from this endeavor. We showed that the preferred orientation of collagen fibers in a 512 x 512 can be determined in ~ 100 ms.This presents a ~10x improvement in the computation time compared to the previously discussed CPU-based image analyzing modality. As proof-of-concept this modality was used to analyze consecutive frames of two videos of 10 and 33 frames per second, respectively. In the first case the GPU-based system successfully captured and analyzed all the frames of the video, while in the

second case it succeed in capturing one in every three frame. Based on the frame rate of the videos, this validates the ~100 ms computation times obtained during analysis. In contrast, the same analysis using a standard CPU failed to capture all but the first frame in both the videos, as expected due to its ~ 950 ms computation times. Both approaches were again compared for a video of SHG images from more complex, collagen-based structures, with the GPU-based method clearly outperforming the standard method. This improvement in processing time makes our approach attractive to other nonlinear imaging modalities that are modified for quantitative analysis.

We believe that our dynamic quantitative imaging approach has potential application to real-time imaging of other noncentrosymmetric biological structures such as observing the perturbation of dendrites and axons in neurons[40]. Additionally, this method would be beneficial for *in vivo* imaging applications[23, 25], where real-time quantitative information is pertinent in obtaining accurate information.

Appendix A

Calculating preferred orientation

The estimation of the preferred orientation of an image grid is carried out in the following steps :

i. In the first step, a horizontal ($dI_{x\,(i,j)}$) and vertical ($dI_{y\,(i,j)}$) intensity gradient is calculated for each pixel. The method used is best demonstrated with the help of a 3 x 3 pixel image block, schematically displayed in Fig. A.1. Based on the location of each pixel within the image block, a centered, forward or a backward difference method is used to calculate the intensity gradient in the horizontal (x-axis) and the vertical (y-axis) direction. The relevant formulae are given in Table A.1, where *i* and *j* refers to the x and y-coordinate of the pixel location, respectively, while *h* represents each pixel width. As an example the intensity gradient for the pixel located in (1,3) can be considered. In this case, the forward difference method is used to calculate the intensity gradient in the horizontal direction, utilizing the intensities of pixels 1 and 2 - $I_{(1,3)}$and $I_{(2,3)}$. Using a similar reasoning, the backward difference method is used to calculate the intensity gradient in the vertical direction by using the intensities of pixels located in (1,2) and (1,3). But in case of the pixel located in (2,2) the centered difference method was used to calculate intensity gradient in both the horizontal and vertical direction. Here, to calculate $dI_{x\,(2,2)}$ we have utilized the intensities $I_{(1,2)}$ and$I_{(3,2)}$, while intensities of pixels located in (2,1) and (2,3) were used for calculating $dI_{y\,(2,2)}$.

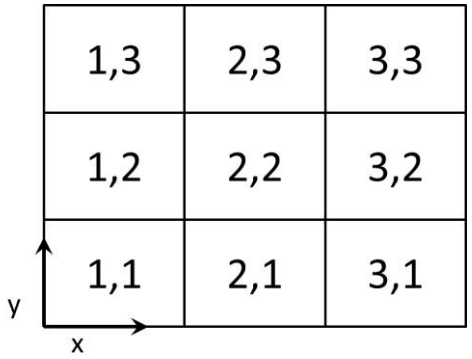

Fig A.1 : Schematic diagram of a 3x3 pixel image block.

Table A.1: Formulae used for calculating intensity gradients of image pixels

Gradients	**Centered Difference**	**Forward Difference**	**Backward Difference**
$dI_{x\,(i,j)}$	$dI_x = \frac{I_{(i+1,j)} - I_{(i-1,j)}}{2h}$	$dI_x = \frac{I_{(i+1,j)} - I_{(i,j)}}{h}$	$dI_x = \frac{I_{(i,j)} - I_{(i-1,j)}}{h}$
$dI_{y\,(i,j)}$	$dI_y = \frac{I_{(i,j+1)} - I_{(i,j-1)}}{2h}$	$dI_y = \frac{I_{(i,j+1)} - I_{(i,j)}}{h}$	$dI_y = \frac{I_{(i,j)} - I_{(i,j-1)}}{h}$

ii. The angular orientation, θ, of each pixel is calculated using,

$$\theta = tan^{-1}\frac{dI_y}{dI_x} \qquad (1)$$

iii. The preferred orientation for each block is calculated using the angular orientation of each of its constituent pixels. The procedure is best explained with an example. Here an image block of 5 pixels is considered with arbitrary angular orientation values for each pixel. The angular orientations are displayed in Table A.2 and the orientation is depicted graphically as orientation lines in Fig. A.2.

Table A.2: Angular orientation of pixels in an image block

Pixel number	**Angular orientation, θ (rad)**
1	0.52
2	2.1
3	2.36
4	-2.61
5	1.92

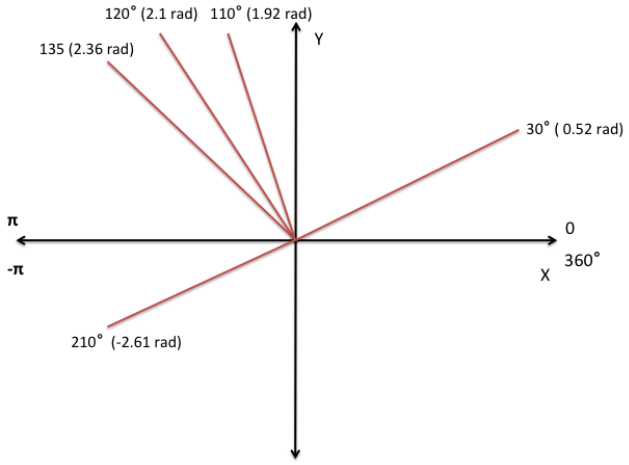

Fig A.2: Angular orientation of the pixels in an image block, represented in a Cartesian co-ordinate system

For clarity in visualization, any angular orientation in the 3rd and 4th quadrant is shifted to the first quadrant. In this example, the angular orientation of pixel 4 (-2.61 rad) is in the 3rd quadrant, so it is shifted by $-\pi$ to the 1st quadrant. The new set of angular orientation values are mentioned in Table A.3, and displayed graphically in Fig. A.3.

Table A.3: Angular orientation of pixels in the 1st and 2nd quadrants

Pixel No	**Angular orientation,θ (rad)**
1	0.52
2	2.1
3	2.36
4	**0.52**
5	1.92

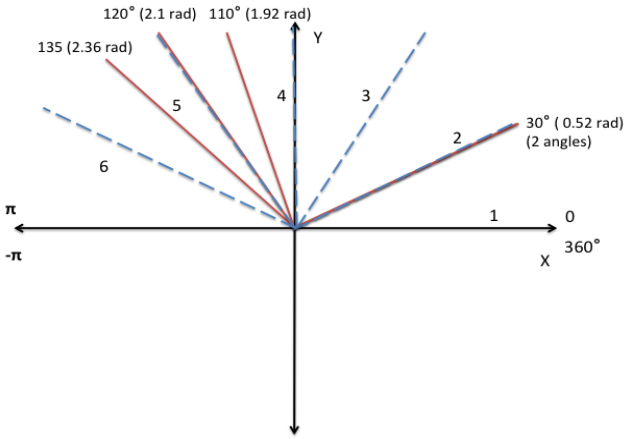

Fig A.3: The angular orientation of all pixels are shifted to the 1st and 2nd quadrant and the angular domain of 0 to π is divided into n regions (n = 6 in this case).

Next, the angular domain of 0 to $\boldsymbol{\pi}$ is divided into 6 equally spaced regions. Figure A.3 shows the regional divisions by dotted blue lines along with the original orientation lines. The number of regions chosen is based on the level of accuracy required in the calculation of circular variance. For each region, a separate set of angular orientation data is obtained. Here, the lower of the two orientation lines are denoted as the division line (θ) and any pixel with its orientation below θ is shifted by π, while, any orientation value above $(\theta + \pi)$ is shifted by $-\pi$. It should be noted that this step does not change the angular orientation, rather expresses it in a different angular domain. After this step the changed set of angular orientations for all the regions are shown in Table A.4. As an example, for set 5, the division line is 2.10 rad. So, the first three pixels of is observed to fall below the division line. So, the angular orientation values of 0.52, 0.52 and 1.92 were shifted by π to 3.66, 3.66 and 5.06 as shown in Table A.4 and Fig. A.4.

Table A.4: Six sets of angular orientation for six divisions

Pixels		**1**	**2**	**3**	**4**	**5**
Sets	**Division line (rad)**	**Angular orientation, θ (rad)**				
1	0	0.52	0.52	1.92	2.10	2.36
2	0.53	0.52	0.52	1.92	2.10	2.36
3	1.06	3.66	3.66	1.92	2.10	1.36
4	1.59	3.66	2.66	1.92	2.10	2.36
5	2.10	3.66	3.66	5.06	2.10	2.36
6	2.65	3.66	3.66	5.06	5.24	5.50

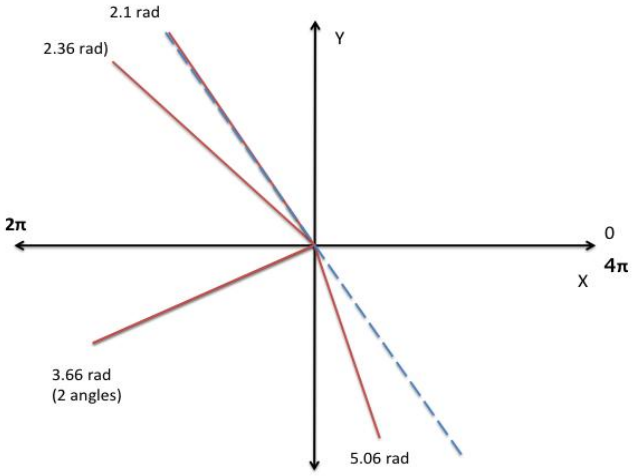

Fig A.4: Angular orientation for set 5 corresponding to a division line of 2.1 radians. For this set the angular orientations for each pixel falls within a region of $2.10<\theta<(2.10+\pi)$.

iv. In the next step, the circular variance is calculated. A detailed discussion of this procedure is provided elsewhere [37, 38]. Briefly, for each set, the angular orientations are expressed in the complex form, $(Aexp^{(i\theta)})$. As only the angular orientation is of importance, the amplitude A is considered 1 for all cases.

$$e^{i\theta} = cos\theta + i\, sin\theta \quad (2)$$

$$\sum e^{i\theta} = \sum cos\theta + i \sum sin\theta \quad (3)$$

The circular variance is calculated using the following formula,

$$C = 1 - R \quad (4)$$

where,

$$R = \frac{1}{n} \times (\sum cos^2\theta + \sum sin^2\theta) \quad (5)$$

The circular variance for the 6 sets of angular orientations in this case is shown in Table A.5.

Table A.5: Calculated Variance

Sets	**1**	**2**	**3**	**4**	**5**	**6**
Circular Variance	0.2989	0.2989	0.2748	0.2748	0.4727	0.2989

v. Finally, the mean angular orientation is calculated for each set individually. All the mean orientation values obtained for the different transformed sets, correspond to the same original set of angular orientations. However, the mean with the lowest circular variance is identified as the preferred orientation. It is seen in Table A.5, the 3rd and 4th set has the lowest variance in this case. If the mean orientation for these two sets are calculated, they are observed to be the same value of 2.71 rad or ~155°. This value is defined as the preferred orientation for the given set of angular orientations.

Appendix B

List of supplemental materials

- **Media 3.1:** Video depicting dynamic quantitative-SHG imaging of a densely packed (stained) tendon sample, as it is scanned by moving the stage laterally in 5 μm steps. 1.2 s image acquisition time was used per location.

- **Media 3.2:** Video displaying dynamic quantitative-SHG imaging of a sparsely distributed (unstained) scaffold sample, as it isscanned by moving the stage laterally in 5 μm steps. The image acquisition time was 1.2 s per location.

- **Media 3.3:** Video showcasing quantitative-SHG imaging of a collagen gel solution in real time, as it dries at room temperature (~ 23º C) over a period of 30 min.

- **Media 3.4:** Video displaying dynamic quantitative SHG imaging of breast tissue microarray cores, as it isscanned by moving the stage laterally in 5 μm steps. The cores contain healthy and malignant tissues and is displayed with a gridded overlay map.

- **Media 4.1:** Video showing a compilation of the results obtained by applying the CPU-based and GPU-based image analysis techniques on a video of SHG images. The video has a frame rate of 10 frames per second (fps) and containsSHG images of breast tissue collagen fibers that are progressively rotated by 20 º with respect to the horizontal. The frames that are succesfully analyzed by the two modalities are displayed.

- **Media 4.2:** Video showing a compilation of the results obtained by applying the CPU-based and GPU-based image analysis techniques on a video of SHG images. The images are obtained from collagen fibers of breast tissue samples, and are progressively rotated by 20º with respect to the horizontal. The video containing the imageshas a frame rate of 33 frames per second (fps). It is demonstrated here that, as the video frame rate was increased, the GPU-based technique fails to capture 2 out of 3 three frames, which is consistent with the computational time previously observed for this technique.

- **Media 4.3:** Video showing a collection of the results obtained by applying the CPU-based and GPU-based image analysis techniques on a video of SHG images. The SHG images are obtained from a variety of collagen based tissues, namely the cervix, tendon and breast biopsy tissues. The goal is to evaluate the performance of the GPU-based code when the SHG images vary in fiber density, orientation and organization.

References

1. P. A. Franken, A. E. Hill, C. W. Peters, and G. Weinreich, "Generation of Optical Harmonics," Phys. Rev. Lett. **7**, 118-119 (1961).
2. J. N. Gannaway, and C. J. R. Sheppard, "Second-harmonic imaging in the scanning optical microscope," Opt. Quant. Electron. **10**, 435-439 (1978).
3. R. Hellwarth, and P. Christensen, "Nonlinear optical microscopic examination of structure in polycrystalline ZnSe," Optics Communications **12**, 318-322 (1974).
4. P. J. Campagnola, and L. M. Loew, "Second-harmonic imaging microscopy for visualizing biomolecular arrays in cells, tissues and organisms," Nat. Biotechnol. **21**, 1356-1360 (2003).
5. M. Strupler, A. M. Pena, M. Hernest, P. L. Tharaux, J. L. Martin, E. Beaurepaire, and M. C. Schanne-Klein, "Second harmonic imaging and scoring of collagen in fibrotic tissues," Opt. Express **15**, 4054-4065 (2007).
6. F. Tiaho, G. Recher, and D. Rouède, "Estimation of helical angles of myosin and collagen by second harmonic generation imaging microscopy," Opt. Express **15**, 12286-12295 (2007).
7. T. Y. Lau, H. K. Sangha, E. K. Chien, B. L. McFarlin, A. J. Wagoner Johnson, and K. C. Toussaint, "Application of Fourier transform-second-harmonic generation imaging to the rat cervix," J. Microsc. **251**, 77-83 (2013).
8. M. Sivaguru, S. Durgam, R. Ambekar, D. Luedtke, G. Fried, A. Stewart, and K. C. Toussaint, "Quantitative analysis of collagen fiber organization in injured tendons using Fourier transform-second harmonic generation imaging," Opt. Express **18**, 24983-24993 (2010).
9. R. Ambekar, M. Chittenden, I. Jasiuk, and K. C. Toussaint, "Quantitative second-harmonic generation microscopy for imaging porcine cortical bone: Comparison to SEM and its potential to investigate age-related changes," Bone **50**, 643-650 (2012).
10. R. Ambekar, T.-Y. Lau, M. Walsh, R. Bhargava, and K. C. Toussaint, "Quantifying collagen structure in breast biopsies using second-harmonic generation imaging," Biomed. Opt. Express **3**, 2021-2035 (2012).

11. C. M. O. Y. Wang, M. C. Oliviera, M. S. Islam, A. Ortega and B. H. Park, "GPU accelerated real-time multi-functional spectral domain optical coherence tomography system at 1300 nm," Opt Express **20**, 17 (2012).
12. N. H. Cho, U. Jung, S. Kim, W. Jung, J. Oh, H. W. Kang, and J. Kim, "High speed SD-OCT system using GPU accelerated mode for in vivo human eye imaging," Journal of the Optical Society of Korea **17**, 68-72 (2013).
13. J. Li, P. Bloch, J. Xu, M. V. Sarunic, and L. Shannon, "Performance and scalability of Fourier domain optical coherence tomography acceleration using," Applied Optics **50**, 1832-1838 (2011).
14. A. J. B. Alberts, L. Julian, R. Martin, R. Keith and W. Peter, , *Molecular Biology of the Cell* (Garland Science, 2007).
15. P. Fratzl, *Collagen: Structure and Mechanics* (Springer, 2008).
16. R. Ambekar Ramachandra Rao, M. R. Mehta, and J. K. C. Toussaint, "Quantitative analysis of biological tissues using Fourier transform-second-harmonic generation imaging," 75692G-75692G (2010).
17. M. F. Young, "Bone matrix proteins: their function, regulation, and relationship to osteoporosis," Osteoporosis international : a journal established as result of cooperation between the European Foundation for Osteoporosis and the National Osteoporosis Foundation of the USA **14 Suppl 3**, S35-42 (2003).
18. J. Caetano-Lopes, A. Nery, H. Canhao, J. Duarte, R. Cascao, A. Rodrigues, I. Perpetuo, S. Abdulghani, P. Amaral, S. Sakaguchi, Y. Konttinen, L. Graca, M. Vaz, and J. Fonseca, "Chronic arthritis leads to disturbances in the bone collagen network," Arthritis Research & Therapy **12**, R9 (2010).
19. N. Morishige, N. Yamada, S. Teranishi, T. Chikama, T. Nishida, and A. Takahara, "Detection of subepithelial fibrosis associated with corneal stromal edema by second harmonic generation imaging microscopy," Investigative Ophthalmology and Visual Science **50**, 3145-3150 (2009).
20. P. Stoller, B. M. Kim, A. M. Rubenchik, K. M. Reiser, and L. B. Da Silva, "Polarization-dependent optical second-harmonic imaging of a rat-tail tendon," Journal of Biomedical Optics **7**, 205-214 (2002).

21. P. J. Su, W. L. Chen, T. H. Li, C. K. Chou, T. H. Chen, Y. Y. Ho, C. H. Huang, S. J. Chang, Y. Y. Huang, H. S. Lee, and C. Y. Dong, "The discrimination of type I and type II collagen and the label-free imaging of engineered cartilage tissue," Biomaterials **31**, 9415-9421 (2010).
22. R. A. Rao, M. R. Mehta, and K. C. Toussaint, "Fourier transform-second-harmonic generation imaging of biological tissues," Opt. Express **17**, 14534-14542 (2009).
23. S. H. Huang, C. D. Hsiao, D. S. Lin, C. Y. Chow, C. J. Chang, and I. Liau, "Imaging of zebrafish In Vivo with second-harmonic generation reveals shortened sarcomeres associated with myopathy induced by statin," PLoS ONE **6** (2011).
24. B. Cohen, "Biological imaging: Beyond fluorescence," Nature **467**, 407-408 (2010).
25. P. Pantazis, J. Maloney, D. Wu, and S. E. Fraser, "Second harmonic generating (SHG) nanoprobes for in vivo imaging," Proc. Natl. Acad. Sci. USA **107**, 14535-14540 (2010).
26. R. LaComb, O. Nadiarnykh, and P. J. Campagnola, "Quantitative Second Harmonic Generation Imaging of the Diseased State Osteogenesis Imperfecta: Experiment and Simulation," Biophys. J. **94**, 4504-4514 (2008).
27. C. Xiyi, N. Oleg, P. Sergey, and J. C. Paul, "Second harmonic generation microscopy for quantitative analysis of collagen fibrillar structure," Nat. Protoc. **7**, 654-669 (2012).
28. T. Hompland, A. Erikson, M. Lindgren, T. Lindmo, and C. de Lange Davies, "Second-harmonic generation in collagen as a potential cancer diagnostic parameter," J. Biomed. Opt. **13**, 054050-054050 (2008).
29. P. G. Ellingsen, M. B. Lilledahl, L. M. S. Aas, C. D. L. Davies, and M. Kildemo, "Quantitative characterization of articular cartilage using Mueller matrix imaging and multiphoton microscopy," J. Biomed. Opt. **16** (2011).
30. M. Lilledahl, O. Haugen, C. de Lange Davies, and L. Svaasand, "Characterization of vulnerable plaques by multiphoton microscopy," J. Biomed. Opt. **12**, 044005 (2007).
31. M. B. Lilledahl, D. M. Pierce, T. Ricken, G. A. Holzapfel, and C. D. L. Davies, "Structural analysis of articular cartilage using multiphoton microscopy: Input for biomechanical modeling," IEEE Trans. Med. Imag. **30**, 1635-1648 (2011).
32. T. Y. Lau, R. Ambekar, and K. C. Toussaint, "Quantification of collagen fiber organization using three-dimensional Fourier transform-second-harmonic generation imaging," Opt. Express **20**, 21821-21832 (2012).

33. R. A. R. Rao, M. R. Mehta, S. Leithem, and J. K. C. Toussaint, "Quantitative analysis of forward and backward second-harmonic images of collagen fibers using Fourier transform second-harmonic-generation microscopy," Opt. Lett. **34**, 3779-3781 (2009).
34. C. B. Raub, V. Suresh, T. Krasieva, J. Lyubovitsky, J. D. Mih, A. J. Putnam, B. J. Tromberg, and S. C. George, "Noninvasive Assessment of Collagen Gel Microstructure and Mechanics Using Multiphoton Microscopy," Biophys. J. **92**, 2212-2222 (2007).
35. R. Gonzalez, and R. Woods, *Digital Image Processing (3rd Edition)* (Prentice Hall, 2007).
36. G. Stockman, and L. G. Shapiro, *Computer Vision* (Prentice Hall PTR, 2001).
37. N. I. Fisher, *Statistical Analysis of Circular Data* (Cambridge University Press, Cambridge, 1995).
38. A. S. S. R. Jammalamadaka, *Topics in Circular Statistics* (World Scientific, Singapore, 2001).
39. S. Tokutake, Y. Imanishi, and M. Sisido, "Efficiency of Second Harmonic Generation from Amino Acids, Peptides, and Polypeptides Carrying Polarizable Aromatic Groups," Mol. Cryst. Liq. Cryst. **170**, 245-257 (1989).
40. D. A. Dombeck, K. A. Kasischke, H. D. Vishwasrao, M. Ingelsson, B. T. Hyman, and W. W. Webb, "Uniform polarity microtubule assemblies imaged in native brain tissue by second-harmonic generation microscopy," Proceedings of the National Academy of Sciences of the United States of America **100**, 7081-7086 (2003).
41. M. M. Kabir, V. V. G. Krishna Inavalli, T. Y. Lau, and K. C. Toussaint Jr, "Application of quantitative second-harmonic generation microscopy to dynamic conditions," Biomedical Optics Express **4**, 2546-2554 (2013).
42. L. A. Flores, V. Vidal, P. Mayo, F. Rodenas, and G. Verdú, "Parallel CT image reconstruction based on GPUs," Radiation Physics and Chemistry **95**, 247-250 (2014).
43. M. A. Bruce, and M. J. Butte, "Real-time GPU-based 3D Deconvolution," Optics Express **21**, 4766-4773 (2013).
44. N. Corporation, "CUDA Programming Guide 5.0," (2014).